

A general method to improve fluorophores for live-cell and single-molecule microscopy

Jonathan B Grimm¹, Brian P English¹, Jiji Chen¹, Joel P Slaughter¹, Zhengjian Zhang¹, Andrey Revyakin^{1,2}, Ronak Patel¹, John J Macklin¹, Davide Normanno^{1,3}, Robert H Singer^{1,4}, Timothée Lionnet¹ & Luke D Lavis¹

Specific labeling of biomolecules with bright fluorophores is the keystone of fluorescence microscopy. Genetically encoded self-labeling tag proteins can be coupled to synthetic dyes inside living cells, resulting in brighter reporters than fluorescent proteins. Intracellular labeling using these techniques requires cell-permeable fluorescent ligands, however, limiting utility to a small number of classic fluorophores. Here we describe a simple structural modification that improves the brightness and photostability of dyes while preserving spectral properties and cell permeability. Inspired by molecular modeling, we replaced the *N,N*-dimethylamino substituents in tetramethylrhodamine with four-membered azetidine rings. This addition of two carbon atoms doubles the quantum efficiency and improves the photon yield of the dye in applications ranging from *in vitro* single-molecule measurements to super-resolution imaging. The novel substitution is generalizable, yielding a palette of chemical dyes with improved quantum efficiencies that spans the UV and visible range.

Fluorescence imaging of specific intracellular molecules requires precise labeling with bright, photostable fluorophores. Genetically encoded fluorophores (GFP and variants) excel with regard to their genetic specificity of labeling¹ but lack the requisite photostability for single-molecule microscopy and other photon-intensive imaging paradigms². Over the past two decades, a number of alternative labeling strategies have been developed that combine the genetic specificity of fluorescent proteins with the favorable photophysics of small-molecule fluorophores. These include FLAsH³, enzyme-based ‘self-labeling tags’ (for example, Snap-tag⁴ and HaloTag^{5,6}), electrophilic ligand–receptor pairs (for example, trimethoprim (TMP) tag⁷ and coumarin–photoactive yellow protein (PYP)⁸) and lipoic acid ligase variants⁹. In particular, the self-labeling tags have enabled advanced imaging experiments, such as super-resolution microscopy^{7,10,11} and biomolecular tracking at single-molecule resolution^{12,13} inside living cells.

Although the general collection of chemical dyes is extensive^{14–16}, relatively few exhibit the cell permeability needed for intracellular labeling. Thus, the available palette of intracellular

self-labeling tag ligands has been limited to classic, net-neutral fluorophores based on coumarin and rhodamine scaffolds^{4–6,17,18}, which exhibit excellent membrane permeability and rapid labeling kinetics but suboptimal brightness and photostability. Previous campaigns to improve dye performance (for example, Cy, Alexa Fluor), involved substantial modifications such as structural rigidification and addition of sulfonate groups^{19–21}. These efforts resulted in highly polar, cell-impermeant dyes, useful *in vitro*²² or on the cell exterior²³ but incompatible with live-cell intracellular applications.

We sought, and now report, a general strategy to improve the brightness of fluorophores through a minimal structural change, thereby preserving cell permeability and efficiency of intracellular labeling. Using molecular modeling as a basis, we replaced the *N,N*-dimethyl group in the classic dye tetramethylrhodamine (TMR) with a four-membered azetidine ring. This minor alteration—a net addition of two carbon atoms—elicited a large increase in quantum yield relative to that of the parent fluorophore, enabling prolonged observations of single molecules in tracking experiments and localization microscopy with improved spatial resolution. We expanded this strategy to other fluorophores including the coumarin, naphthalimide, acridine, rhodol, carborrhodamine, oxazine and Si-rhodamine classes, in which the straightforward replacement of *N,N*-dialkylamino groups with azetidines also increased quantum yield. This general method allowed for substantial improvements in fluorophore brightness while preserving the requisite small size and high membrane permeability for use in live cells.

RESULTS

Rational design of an improved tetraalkylrhodamine dye

The simplest rhodamine fluorophore, rhodamine 110 (**1**; Fig. 1a), exhibits an absorption maximum in the blue ($\lambda_{\text{max}} = 497 \text{ nm}$) with a large extinction coefficient ($\epsilon = 7.6 \times 10^4 \text{ M}^{-1} \text{ cm}^{-1}$), emission maximum in the green ($\lambda_{\text{em}} = 520 \text{ nm}$) and a high quantum yield ($\phi = 0.88$) (ref. 24). Alkylation of the rhodamine elicits a bathochromic shift in absorption and fluorescence emission wavelengths. For example, TMR (**2**) displayed $\lambda_{\text{max}}/\lambda_{\text{em}} = 548 \text{ nm}/572 \text{ nm}$ and $\epsilon = 7.8 \times 10^4 \text{ M}^{-1} \text{ cm}^{-1}$ (Fig. 1a). This shift in spectral

¹Janelia Research Campus, Howard Hughes Medical Institute, Ashburn, Virginia, USA. ²Department of Biochemistry, University of Leicester, Leicester, UK. ³Laboratoire Physico-Chimie Curie, Institut Curie, Paris, France. ⁴Department of Anatomy and Structural Biology, Albert Einstein College of Medicine, Bronx, New York, USA. Correspondence should be addressed to T.L. (lionnet@janelia.hhmi.org) or L.D.L. (lavis@janelia.hhmi.org).

RECEIVED 8 APRIL 2014; ACCEPTED 8 DECEMBER 2014; PUBLISHED ONLINE 19 JANUARY 2015; DOI:10.1038/NMETH.3256

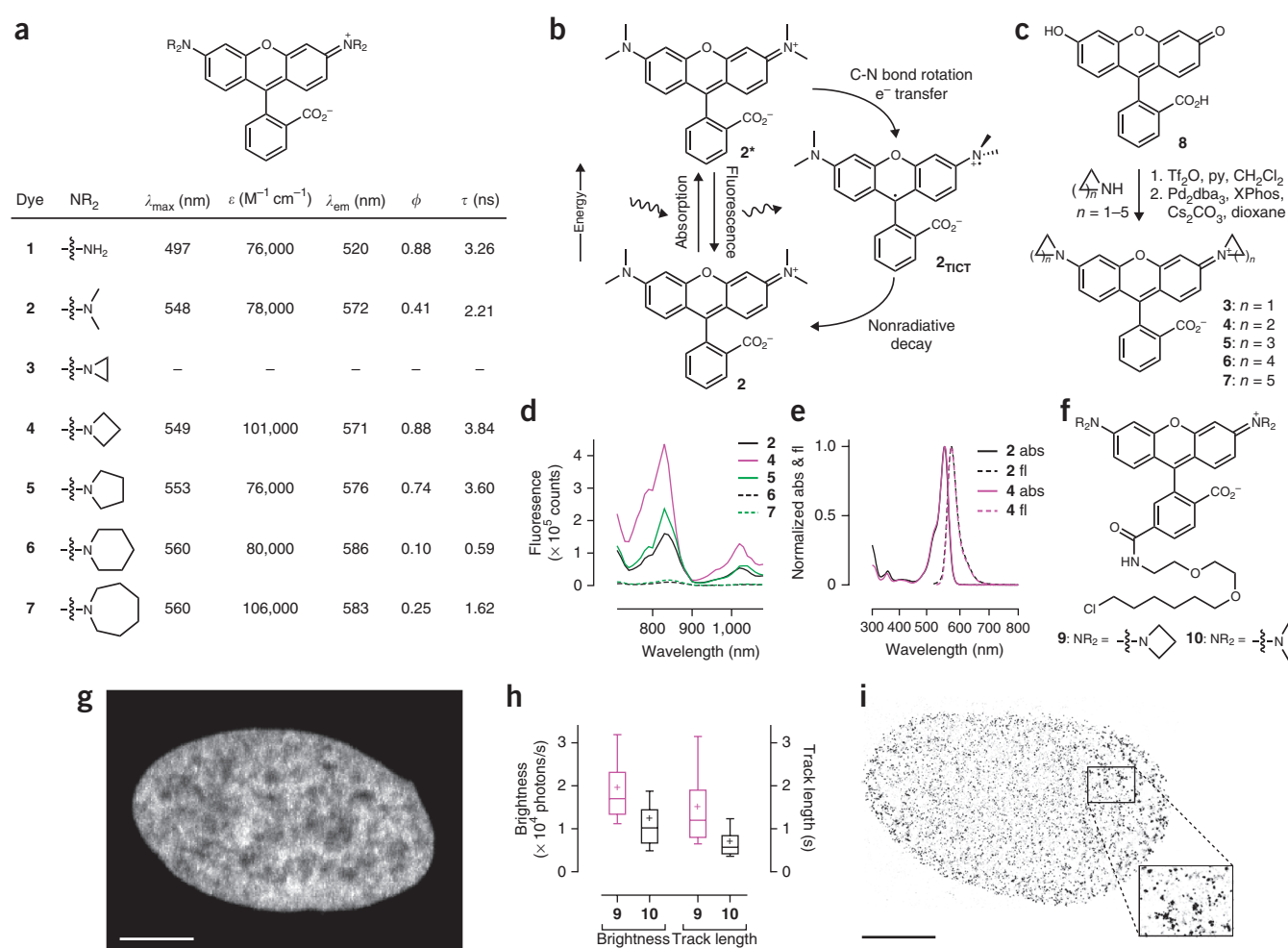


Figure 1 | Development and utility of JF₅₄₉. **(a)** Spectroscopic data for rhodamines 1–7. λ_{max} , absorption maximum; ϵ , extinction coefficient; λ_{em} , emission maximum; ϕ , quantum yield; τ , fluorescence lifetime. Compound 3 did not show appreciable visible absorption or fluorescence. **(b)** Jablonski diagram showing the process of twisted internal charge transfer (TICT). **(c)** Synthesis of rhodamines 3–7 from fluorescein (8) using palladium-catalyzed cross-coupling. **(d)** Two-photon excitation spectra of fluorophores 2 and 4–7. **(e)** Normalized absorption (abs) and fluorescence emission (fl) spectra for TMR (2) and JF₅₄₉ (4). **(f)** Chemical structure of JF₅₄₉-HaloTag ligand 9 and TMR-HaloTag ligand 10. **(g)** Confocal maximum projection image of nucleus from a live, washed HeLa cell expressing HaloTag-H2B and incubated with JF₅₄₉-HaloTag ligand 9; scale bar, 5 μm . **(h)** Whisker plot comparing brightness ($n > 4,000$) and track length ($n > 500$) of HaloTag-H2B molecules labeled with ligand 9 or 10; cross indicates mean; whiskers span 10th–90th percentile. **(i)** dSTORM fluorescence microscopy image of the nucleus of a fixed U2OS cell expressing HaloTag-H2B and labeled with JF₅₄₉ ligand 9. The dSTORM image is composed of 10,000 consecutive frames, and the 44,937 detected particles are displayed according to their localization full-width at half-maximum. The mean localization error was 17.2 nm, and the median localization error was 14.1 nm; enlarged region is magnified twofold; scale bar, 5 μm .

properties is accompanied by a large decrease in quantum yield, with TMR showing $\phi = 0.41$ in aqueous solution. Both of these dyes are used in commercial self-labeling tag substrates and can be used to label intracellular and extracellular proteins in living cells.

A plausible explanation for the lower quantum efficiency of *N,N,N',N'*-tetraalkylrhodamines such as 2 is the formation of a twisted internal charge transfer (TICT) state. In this process fluorophore 2 absorbs a photon to give an excited state (2*, Fig. 1b), which is followed by electron transfer from the nitrogen atom to the xanthen ring system with concomitant twisting of the C_{aryl}-N bond (2^{TICT}). TICT is energetically favorable in tetraalkylrhodamine dyes owing to the lower ionization potential of *N,N*-dialkylanilines versus less substituted anilines²⁵. The TICT form relaxes without emission of a photon, leading to rapid nonradiative decay of the excited state^{25–27}. The 2^{TICT} diradical intermediate may also undergo irreversible bleaching reactions²⁷.

Thus, rhodamine derivatives in which TICT is disfavored should exhibit increased quantum efficiency, longer fluorescence lifetimes and higher photostability.

On the basis of this hypothesis, we reasoned that replacing the *N,N*-dimethyl group in TMR (2) with differently sized nitrogen-containing rings (ranging from aziridine to azepane, compounds 3–7; Fig. 1a) might mitigate TICT and improve fluorescence properties. Although previous work had shown the pyrrolidine-containing rhodamine 5 to have a higher fluorescence brightness than the piperidino-rhodamine 6 (refs. 25,28), azacyclic rhodamines with smaller or larger ring sizes (3, 4 and 7) had not been explored. From quantum mechanical calculations, we predicted that the novel azetidiny rhodamine 4 would exhibit superior brightness to TMR (2) and the other alkylated rhodamines 3, 5, 6 and 7 (Supplementary Note).

To test this prediction we synthesized compounds 3–7 from fluorescein (8) using a palladium-catalyzed cross-coupling

approach²⁸ (Fig. 1c and Supplementary Note). We then evaluated the photophysical properties of compounds 3–7 in aqueous solution, comparing them to known rhodamines 1 and 2 (Fig. 1a and Supplementary Fig. 1a). Aziridine derivative 3 gave a colorless solution with no discernible fluorescence, a result suggesting that the ring strain in the aziridine substituents forces the rhodamine molecule to adopt a colorless, nonfluorescent lactone form. Compounds 4–7 had λ_{max} and λ_{em} values similar to those of TMR (2), with increased ring size causing a slight bathochromic shift of up to 10 nm. Compounds 4 and 7 had ϵ values ~30% higher than those of the other dyes; values of this magnitude have been observed with tetraethylrhodamine^{15,28}.

Although the λ_{max} , λ_{em} , and ϵ of the different rhodamine dyes showed only modest dependence on substituent ring size, the fluorescence lifetime (τ) and ϕ varied widely as a function of molecular structure (Fig. 1a). Rhodamine 4 exhibited a high quantum yield value ($\phi = 0.88$) and long fluorescence lifetime ($\tau = 3.8$ ns), larger than the values for TMR (2; $\phi = 0.41$, $\tau = 2.2$ ns) and similar to the parent rhodamine 110 (1; $\phi = 0.88$, $\tau = 3.3$ ns). Rhodamine 4 was also 60% brighter ($\epsilon \times \phi$) than the pyrrolidine derivative 5, which had $\phi = 0.74$ and $\tau = 3.6$ ns. The piperidine derivative 6 showed a sharp decrease in fluorescence with $\phi = 0.10$ and $\tau = 0.6$ ns; the lifetime values for 5 and 6 were consistent with those measured for similar fluorophores²⁵. Rhodamine 7 gave slightly higher values of $\phi = 0.25$ and $\tau = 1.62$ ns relative to 6, suggesting that the increased flexibility of this larger ring can offset the other deleterious structural effects on rhodamine fluorescence.

The improved brightness of rhodamine 4 under one-photon excitation (Fig. 1a) extended to two-photon excitation (Fig. 1d and Supplementary Fig. 1b). This enhancement is brought about by a negligible structural change—the addition of two carbon atoms—that preserves many of the desirable properties of TMR. For example, the absorption and emission spectra of 2 and 4 are superimposable (Fig. 1e), and the dyes show comparable sensitivity to solvent polarity (Supplementary Fig. 1c), which suggests similar cell permeability^{18,24}. Because of its high brightness, favorable chemical properties and $\lambda_{\text{max}} = 549$ nm, azetidinyl rhodamine 4 was named JF₅₄₉ (Janelia Fluor 549).

Utility of JF₅₄₉ in cellular imaging

To evaluate the performance of the dye as a label, we synthesized JF₅₄₉ HaloTag ligand (9; Fig. 1f) starting from a 6-carboxyfluorescein derivative (Supplementary Note). This molecule is a direct analog of the commercial TMR-based HaloTag ligand 10. We compared the labeling kinetics of compounds 9 and 10 with a novel Cy3 HaloTag ligand and measured the brightness and photon yield of the resulting conjugates. The JF₅₄₉ ligand (9) showed labeling kinetics comparable to those of the TMR ligand (10) and increased brightness relative to that of the other dyes *in vitro* (Supplementary Note). Incubation of live HeLa cells expressing a HaloTag–histone 2B (H2B) fusion with compound 9 resulted in bright nuclear labeling (Fig. 1g) and low cytoplasmic background, thereby demonstrating that the JF₅₄₉ HaloTag ligand can efficiently cross the membrane of live cells and selectively label the HaloTag protein.

Incubation with low amounts of ligand 9 or 10 (<50 nM) allowed imaging of single molecules (Supplementary Video 1) and evaluation of fluorophore brightness (photons/s) and

photostability (i.e., track length) of individual molecules of labeled HaloTag–H2B. The JF₅₄₉ ligand 9 demonstrated a large increase in both brightness and photostability compared to those of TMR ligand 10 (Fig. 1h). Proteins labeled with 10 exhibited a mean value of 1.1×10^4 photons/s and a mean track length of 0.72 s. Conjugates of JF₅₄₉ ligand 9 emitted nearly twice the number of photons per second (1.9×10^4) and lasted about twice as long (mean track length = 1.6 s). This improvement in single-molecule brightness extended to direct stochastic optical reconstruction microscopy (dSTORM) experiments, in which the use of a reducing environment enables the reversible photoswitching of synthetic fluorophores^{7,29–31}. We labeled U2OS cells expressing HaloTag–H2B with JF₅₄₉ ligand 9 or TMR ligand 10. We then fixed the cells and imaged them using standard dSTORM conditions. This resulted in a super-resolution image of H2B using ligand 9 or molecule 10 with median localization errors (σ) of 14.1 nm and 17.0 nm, respectively (Fig. 1i and Supplementary Fig. 2a,b). We could also perform dSTORM inside living cells using the cellular reducing environment to elicit photoswitching of the JF₅₄₉ label⁷ (Supplementary Fig. 2c). Together, our results establish JF₅₄₉ as the best available ligand in this spectral range for HaloTag conjugation *in vitro*, in fixed cells and in live cells, thus validating our fluorophore design strategy.

Extension of the azetidine strategy to other dye scaffolds

After observing the improved brightness with the rhodamine scaffold, we sought to replace *N,N*-dialkyl groups found in other fluorophores with azetidines. The *N,N*-dialkyl motif is found in numerous classic fluorophore scaffolds¹⁴ (Table 1), including coumarins (for example, 11, coumarin 461), naphthalimides, acridines (for example, 17, acridine orange), rhodols, carbodimines²⁴, oxazines (for example, 23, oxazine 1) and Si-rhodamines^{18,32}. TICT has been proposed as a major contributor to nonradiative decay in these fluorescence systems, leading to modest quantum efficiencies²⁶. As with the rhodamine case, we used an efficient palladium-catalyzed cross-coupling approach to install the azetidine motif in these fluorophores, starting from accessible aryl halides or aryl triflates (Supplementary Note).

In all cases the azetidine substitution imparted large increases in quantum yield without substantial deleterious effects on other spectral properties (Table 1 and Supplementary Fig. 3). Coumarin 461 (11) exhibited $\lambda_{\text{max}}/\lambda_{\text{em}} = 372$ nm/470 nm, $\epsilon = 1.8 \times 10^4$ M^{−1} cm^{−1} and a modest $\phi = 0.19$ in aqueous buffer. The analog 12 showed a fivefold increase in quantum yield ($\phi = 0.96$) along with an 18-nm hypsochromic shift in absorbance maxima ($\lambda_{\text{max}} = 354$ nm). The emission spectrum and extinction coefficients of 12 ($\lambda_{\text{max}} = 467$ nm, $\epsilon = 1.5 \times 10^4$ M^{−1} cm^{−1}) were similar to those of the parent dye 11. The widely used 7-(diethylamino)coumarin-3-carboxylic acid (DEAC, 13) displayed $\lambda_{\text{max}}/\lambda_{\text{em}} = 410$ nm/471 nm and $\epsilon = 3.5 \times 10^4$ M^{−1} cm^{−1} but a low quantum yield ($\phi = 0.03$). The azetidinyl analog 14 had a shorter absorption maximum ($\lambda_{\text{max}} = 387$ nm) and a smaller extinction coefficient ($\epsilon = 2.4 \times 10^4$ M^{−1} cm^{−1}). Nonetheless, the emission maxima proved quite similar with $\lambda_{\text{em}} = 470$ nm, and the azetidine substitution increased the quantum yield by almost 30-fold ($\phi = 0.84$).

We then considered the naphthalimide, acridine and rhodol fluorophore scaffolds. Dimethylamino-substituted naphthalimides such as compound 15 are important environmentally sensitive

Table 1 | Spectroscopic data for fluorophores **11–26**

Parent structure	Substitution	λ_{\max} (nm)	ϵ ($M^{-1} \text{ cm}^{-1}$)	λ_{em} (nm)	ϕ
	11: $R_2N = \text{N(CH}_3)_2$	372	18,000	470	0.19
	12: $R_2N = \text{N(CH}_2\text{CH}_2)_2$	354	15,000	467	0.96
	13: $R_2N = \text{N(CH}_3)_2$	410	35,000	471	0.03
	14: $R_2N = \text{N(CH}_2\text{CH}_2)_2$	387	24,000	470	0.84
	15: $R_2N = \text{N(CH}_3)_2$	436	9,500	–	<0.01
	16: $R_2N = \text{N(CH}_2\text{CH}_2)_2$	464	18,000	553	0.28
	17: $R_2N = \text{N(CH}_3)_2$	493	50,000	528	0.21
	18: $R_2N = \text{N(CH}_2\text{CH}_2)_2$	492	47,000	531	0.52
	19: $R_2N = \text{N(CH}_3)_2$	518	60,000	546	0.21
	20: $R_2N = \text{N(CH}_2\text{CH}_2)_2$	519	59,000	546	0.85
	21: $R_2N = \text{N(CH}_3)_2$	606	121,000	626	0.52
	22: $R_2N = \text{N(CH}_2\text{CH}_2)_2$	608	99,000	631	0.67
	23: $R_2N = \text{N(CH}_3)_2$	655	111,000	669	0.07
	24: $R_2N = \text{N(CH}_2\text{CH}_2)_2$	647	99,000	661	0.24
	25: $R_2N = \text{N(CH}_3)_2$	643	141,000 ^a	662	0.41
	26: $R_2N = \text{N(CH}_2\text{CH}_2)_2$	646	152,000 ^a	664	0.54

^aExtinction coefficient measured in ethanol containing 0.1% (v/v) trifluoroacetic acid. λ_{\max} , absorption maximum; ϵ , extinction coefficient; λ_{em} , emission maximum; ϕ , quantum yield.

fluorophores³³ but have not been useful as general fluorescent labels owing to their poor absorbance and fluorescence in water ($\lambda_{\max} = 436 \text{ nm}$, $\epsilon = 9.5 \times 10^3 \text{ M}^{-1} \text{ cm}^{-1}$, $\phi < 0.01$; **Table 1**). We prepared the azetidiny analog **16**, which showed a bathochromic shift in absorbance maximum ($\lambda_{\max} = 464 \text{ nm}$), a larger extinction coefficient ($\epsilon = 1.8 \times 10^4 \text{ M}^{-1} \text{ cm}^{-1}$) and a high quantum yield ($\phi = 0.28$, $\lambda_{\text{em}} = 553 \text{ nm}$). The classic fluorophore acridine orange (**17**) gave $\phi = 0.21$ when measured in aqueous solution, a value consistent with published data³⁴. The azetidine analog **18** was 2.5-fold brighter with $\phi = 0.52$. Other spectral properties of the two acridines were similar. Rhodol (**19**) had $\lambda_{\max}/\lambda_{\text{em}} = 518 \text{ nm}/546 \text{ nm}$, and $\epsilon = 6.0 \times 10^4 \text{ M}^{-1} \text{ cm}^{-1}$ and $\phi = 0.21$, consistent with previous results³⁵. The azetidine-containing analog **20** had nearly indistinguishable λ_{\max} , λ_{em} and ϵ values. However, the replacement of the *N,N*-dimethylamino group in **19** with an azetidine

in **20** gave a fourfold increase in quantum yield ($\phi = 0.85$).

We then turned to longer-wavelength fluorophores. The carbon-containing analog of TMR (**21**) exhibited $\lambda_{\max}/\lambda_{\text{em}} = 606 \text{ nm}/626 \text{ nm}$, $\epsilon = 1.21 \times 10^5 \text{ M}^{-1} \text{ cm}^{-1}$ and $\phi = 0.52$ in aqueous buffer (**Table 1**). The azetidiny carborhodamine **22** had similar absorption and emission maxima ($\lambda_{\max}/\lambda_{\text{em}} = 608 \text{ nm}/631 \text{ nm}$) and extinction coefficient ($\epsilon = 9.9 \times 10^4 \text{ M}^{-1} \text{ cm}^{-1}$) but a higher quantum yield ($\phi = 0.67$). The classic dye oxazine 1 (**23**) had spectral properties in the far red with $\lambda_{\max}/\lambda_{\text{em}} = 655 \text{ nm}/669 \text{ nm}$ and $\epsilon = 1.11 \times 10^5 \text{ M}^{-1} \text{ cm}^{-1}$ but a relatively low $\phi = 0.07$. The azetidine substitution in dye **24** gave a small hypsochromic shift ($\lambda_{\max}/\lambda_{\text{em}} = 647 \text{ nm}/661 \text{ nm}$), a slightly lower extinction coefficient ($\epsilon = 9.9 \times 10^4 \text{ M}^{-1} \text{ cm}^{-1}$) and a 3.4-fold improvement in quantum yield ($\phi = 0.24$). Finally, the recently described silicon-containing TMR^{18,32} (SiTMR, **25**) had $\lambda_{\max}/\lambda_{\text{em}} = 643 \text{ nm}/662 \text{ nm}$ and $\phi = 0.41$; the azetidiny analog **26** gave similar absorption and emission maxima ($\lambda_{\max}/\lambda_{\text{em}} = 646 \text{ nm}/664 \text{ nm}$) and a higher $\phi = 0.54$. Because Si-rhodamines often adopt a colorless form in water^{18,32}, we measured the extinction coefficients in acidic ethanol, finding $\epsilon = 1.41 \times 10^5 \text{ M}^{-1} \text{ cm}^{-1}$ for SiTMR (**25**) and $\epsilon = 1.52 \times 10^5 \text{ M}^{-1} \text{ cm}^{-1}$ for azetidine **26**. Overall, these results demonstrate that the azetidiny substitution is generalizable to different fluorophore scaffolds, producing substantial improvements in quantum yield values.

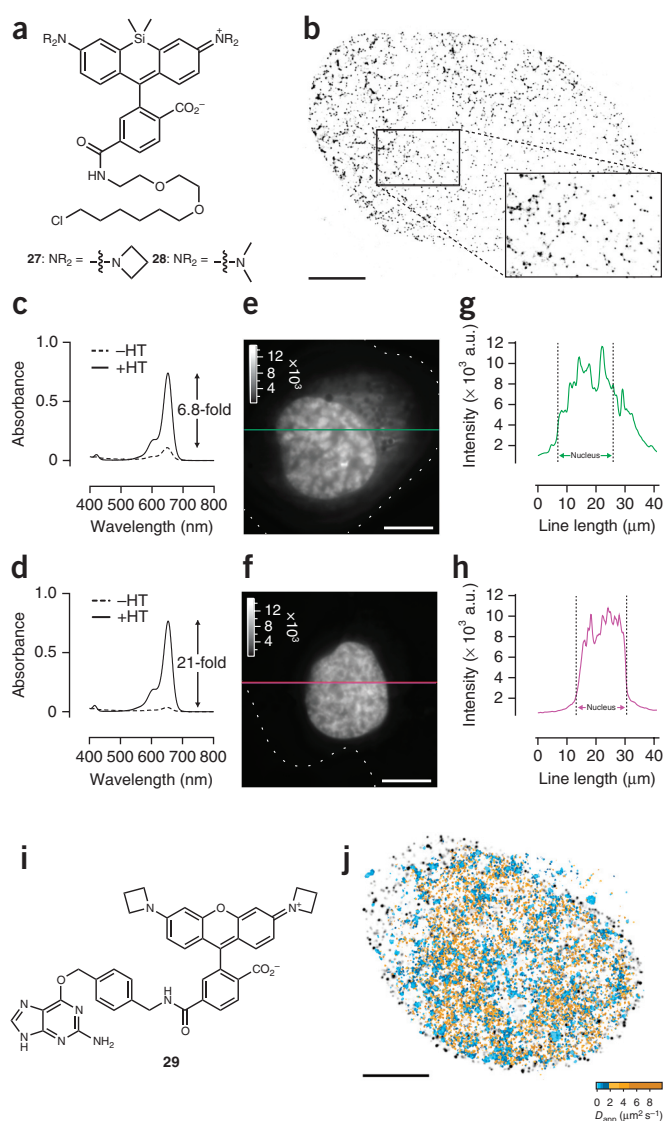
Cellular imaging using azetidiny Si-rhodamine

Compounds based on SiTMR (**25**) were previously reported to be efficient labels for Snap-tag, HaloTag and other proteins inside live cells^{18,32}. Compound **26** had superior brightness ($\epsilon \times \phi$; **Table 1**) relative to that of **25** and was named JF₆₄₆ (Janelia Fluor 646). To compare these two dyes directly in cellular imaging experiments, we synthesized the HaloTag ligand of the azetidiny Si-rhodamine (**27**; **Fig. 2a**) and the known¹⁸ HaloTag ligand of SiTMR (**28**), starting from a novel silafluorescein precursor (**Supplementary Note**). Both Si-rhodamine ligands **27** and **28** were excellent labels for super-resolution dSTORM imaging of HaloTag-H2B in U2OS cells (**Fig. 2b** and **Supplementary Fig. 4a**), showing median localization errors of 8.4 nm and 9.0 nm, respectively (**Supplementary Fig. 4b**). We also performed dSTORM on live HeLa cells expressing HaloTag-tubulin and labeled with JF₆₄₆ ligand **27**. We observed high photon yields and low background with this label, giving a median $\sigma = 7.1 \text{ nm}$ (**Supplementary Fig. 4c–e**).

Figure 2 | Utility of JF₆₄₆ in cellular imaging. **(a)** Chemical structures of JF₆₄₆-HaloTag ligand **27** and SiTMR-HaloTag ligand **28**. **(b)** dSTORM fluorescence microscopy image of a fixed U2OS cell nucleus expressing HaloTag-H2B and labeled with **27**. The dSTORM image is composed of 5,000 consecutive frames, and the 263,415 detected particles are displayed according to their localization full-width at half-maximum. The mean localization error was 11.1 nm, and the median localization error was 8.4 nm; enlarged region is magnified 1.92-fold; scale bar, 5 μ m. **(c,d)** Absorbance spectra of ligands **28** (5 μ M; **c**) and **27** (5 μ M; **d**) in the absence (–HT) and presence (+HT) of excess HaloTag protein. **(e,f)** Wide-field fluorescence microscopy images of live HeLa cells transfected with H2B-HaloTag, incubated with **28** (100 nM; **e**) or **27** (100 nM; **f**) and imaged without intermediate washing steps; dashed lines indicate cellular boundary; scale bars, 10 μ m. **(g)** Plot of line-scan intensity in **e** (green line) as a function of line length. **(h)** Plot of line-scan intensity in **f** (magenta line) as a function of line length. a.u., arbitrary units. **(i)** Chemical structure of JF₅₄₉-Snap-tag ligand **29**. **(j)** Overlay of the dSTORM image of H2B (grayscale) and regions of fast TetR diffusivity (D_{app} ; 2–10 μ m² s^{–1}; yellow) and slow TetR diffusivity (<2 μ m² s^{–1}; blue) in a live U2OS cell.

As noted above, the free Si-rhodamine dyes **25** and **26** exhibited low visible absorption in aqueous solution, which suggests that the dyes preferentially adopt the closed, UV-absorbing, lactone form. However, conjugation to a protein changes the local environment around the dye, eliciting a large increase in absorbance^{18,32}. We compared the chromogenicity of ligands **27** and **28** upon reaction with purified protein and in live-cell imaging experiments. The SiTMR ligand **28** showed an enhancement of 6.8-fold upon reaction with excess HaloTag protein in buffer (Fig. 2c), a result consistent with previous reports¹⁸. The azetidiny Si-rhodamine-HaloTag ligand **27** had lower background, leading to a larger, 21-fold increase in absorbance under the same conditions (Fig. 2d). We then performed ‘no-wash’ imaging experiments using HeLa cells expressing the HaloTag-H2B fusion. Incubation with either ligand (100 nM) followed directly by wide-field imaging gave brightly labeled nuclei using both the SiTMR ligand **28** and the JF₆₄₆ ligand **27** (Fig. 2e,f). However, SiTMR showed substantial extranuclear fluorescence, whereas the JF₆₄₆ ligand exhibited lower nonspecific staining (Fig. 2g,h and Supplementary Fig. 4f). Overall, these results show that the known SiTMR ligand **28** can be replaced with the structurally similar JF₆₄₆ ligand **27** to achieve better localization error in super-resolution imaging and lower background in conventional fluorescence microscopy.

The excellent properties of JF₅₄₉ and JF₆₄₆ and the large spectral separation between the two fluorophores raised the possibility of imaging two distinct protein species at the single-molecule level in the same living cell. To achieve orthogonal labeling, we prepared the Snap-tag ligand of JF₅₄₉ (**29**; Fig. 2i and Supplementary Note). We coexpressed HaloTag-H2B and a fusion of the Snap-tag enzyme and the Tet repressor protein (Snap-tag-TetR) in U2OS cells and labeled the HaloTag-H2B with JF₆₄₆ ligand **27** and the Snap-tag-TetR with JF₅₄₉ ligand **29**. We imaged the trajectories of individual JF₅₄₉-labeled TetR proteins and then performed a rapid live-cell dSTORM experiment of the JF₆₄₆-H2B conjugate (Supplementary Fig. 4g and Supplementary Video 2). This proof-of-concept, two-color experiment revealed the respective partitions of fast- and slow-diffusing DNA-binding protein in relation to the chromatin structure of the nucleus (Fig. 2j) and showed that TetR diffusion is slower in H2B-dense regions (Supplementary Fig. 4h), which



is consistent with previous observations that inert tracers diffuse more slowly in dense chromatin regions³⁶.

Cellular imaging using an azetidiny coumarin label

The improvements to coumarin **13** brought about by the azetidine substitution were also interesting, as derivatives of this cell-permeable dye can be used for intracellular labeling. We compared the performance of a commercial Snap-tag ligand **30** (i.e., Snap-Cell 430; Fig. 3a) to that of novel azetidiny derivative **31**, which we synthesized from coumarin **14** (Supplementary Note). Under identical transient transfection, labeling and imaging conditions, H2B-Snap-tag-expressing HeLa cells were stained with the red fluorescent nuclear stain DRAQ5 and either known ligand **30** or azetidiny ligand **31**. Using the DRAQ5 staining as a spatial reference (Fig. 3b,c), we measured the intensity of individual nuclei labeled by either Snap-tag ligand. Cells incubated with ligand **30** had low fluorescence intensity, whereas cells labeled with **31** exhibited brighter nuclear labeling (Fig. 3d,e). Quantification of nuclear intensity showed that the cells labeled with azetidine **31** had median values that were fivefold higher than those of cells labeled with the commercial compound **30** (Fig. 3f).

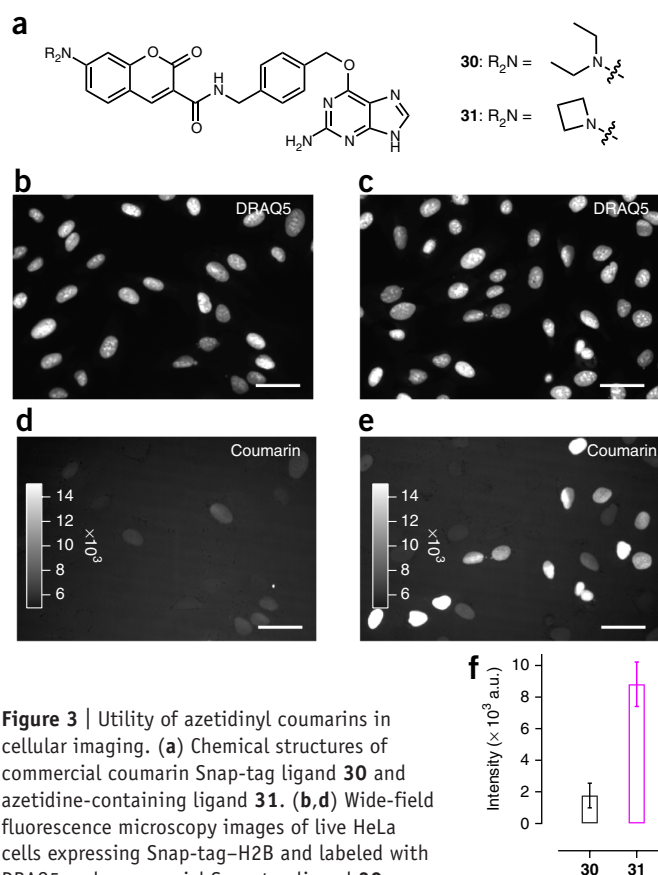


Figure 3 | Utility of azetidiny coumarins in cellular imaging. **(a)** Chemical structures of commercial coumarin Snap-tag ligand **30** and azetidine-containing ligand **31**. **(b,d)** Wide-field fluorescence microscopy images of live HeLa cells expressing Snap-tag-H2B and labeled with DRAQ5 and commercial Snap-tag ligand **30**. **(b)** Fluorescence of DRAQ5 nuclear staining. **(d)** Fluorescence of coumarin **30**-labeled Snap-tag-H2B. **(c,e)** Wide-field fluorescence microscopy image of live HeLa cells expressing Snap-tag-H2B and labeled with DRAQ5 and novel azetidiny coumarin Snap-tag ligand **31**. **(c)** Fluorescence of DRAQ5 nuclear staining. **(e)** Fluorescence of coumarin **31**-labeled Snap-tag-H2B. **(f)** Quantification of the median nuclear fluorescence above background coumarin label in cells when labeled with ligand **30** (black) or **31** (magenta; $n = 50$; error bars, s.e.m.). a.u., arbitrary units. Scale bars, 50 μm .

DISCUSSION

We report a simple structural modification—the replacement of *N,N*-dialkyl groups with azetidines—that improves the quantum efficiency of classic fluorophores with absorbance maxima from the UV to the far red. In particular, the azetidine substitution endows JF₅₄₉ and JF₆₄₆ with superior brightness while retaining excellent cell penetration and fast labeling kinetics with the HaloTag. These novel dyes should facilitate new microscopic experiments such as multiplexed single-molecule measurements at a high spatiotemporal resolution inside living cells (for example, Fig. 2j). Such experiments will constitute a major tool in testing models relating molecular architecture and biological dynamics^{36,37}.

In addition to serving as ligands for self-labeling tags, many classic fluorophores are components of fluorescent labels, stains and indicators^{14,15,21}. Replacement of the dialkylamino groups in these molecules with azetidines could yield a new generation of probes with improved properties. For example, derivatives of the bright coumarin fluorophores **12** and **14** could find use in other protein-based labeling schemes^{8,9} or as non-natural amino acids³⁸, where the size of the fluorophore label is

restricted by the biochemical machinery. This general approach to attenuate nonradiative decay sets the stage for combinatorial enhancements via other structural modifications, such as halogenation³⁹ or attachment of triplet-state quenchers⁴⁰, to further improve brightness and photostability, altogether pushing the limits of biological imaging.

METHODS

Methods and any associated references are available in the [online version of the paper](#).

Note: Any Supplementary Information and Source Data files are available in the online version of the paper.

ACKNOWLEDGMENTS

We thank S. Eddy and E. Betzig for contributive discussions, M. Dahan (Curie Institut) and X. Darzacq (Berkeley) for the Snap-tag-TetR plasmid, M. Tadross (Janelia) for the purified HaloTag protein and W. Hu (Janelia) for cloning and purifying the recombinant HaloTag-MS2 protein. This work was supported by the Howard Hughes Medical Institute. Salary for R.H.S. is funded by US National Institutes of Health grants GM57071, NS83085 and EB13571.

AUTHOR CONTRIBUTIONS

J.B.G. conceived of the project and performed organic synthesis. B.P.E. and J.C. designed and performed cellular microscopy experiments and analyzed data. J.P.S. performed organic synthesis. Z.Z. prepared bioconjugates, performed *in vitro* single-molecule microscopy and analyzed data. A.R. performed *in vitro* single-molecule microscopy and analyzed data. R.P. and J.J.M. performed two-photon spectroscopy and fluorescence lifetime measurements. D.N. designed and validated the Snap-tag-TetR plasmid. R.H.S. interpreted data. T.L. designed experiments and performed data analysis. L.D.L. conceived of the project, performed one-photon spectroscopic measurements and wrote the manuscript with input from the other authors.

COMPETING FINANCIAL INTERESTS

The authors declare competing financial interests: details are available in the [online version of the paper](#).

Reprints and permissions information is available online at <http://www.nature.com/reprints/index.html>.

- Kremers, G.-J., Gilbert, S.G., Cranfill, P.J., Davidson, M.W. & Piston, D.W. Fluorescent proteins at a glance. *J. Cell Sci.* **124**, 157–160 (2011).
- Xia, T., Li, N. & Fang, X. Single-molecule fluorescence imaging in living cells. *Annu. Rev. Phys. Chem.* **64**, 459–480 (2013).
- Griffin, B.A., Adams, S.R. & Tsien, R.Y. Specific covalent labeling of recombinant protein molecules inside live cells. *Science* **281**, 269–272 (1998).
- Keppler, A. *et al.* A general method for the covalent labeling of fusion proteins with small molecules *in vivo*. *Nat. Biotechnol.* **21**, 86–89 (2003).
- Los, G.V. *et al.* HaloTag: a novel protein labeling technology for cell imaging and protein analysis. *ACS Chem. Biol.* **3**, 373–382 (2008).
- Encell, L.P. *et al.* Development of a dehalogenase-based protein fusion tag capable of rapid, selective and covalent attachment to customizable ligands. *Curr. Chem. Genomics* **6**, 55–71 (2012).
- Wombacher, R. *et al.* Live-cell super-resolution imaging with trimethoprim conjugates. *Nat. Methods* **7**, 717–719 (2010).
- Hori, Y., Ueno, H., Mizukami, S. & Kikuchi, K. Photoactive yellow protein-based protein labeling system with turn-on fluorescence intensity. *J. Am. Chem. Soc.* **131**, 16610–16611 (2009).
- Uttamapinant, C. *et al.* A fluorophore ligase for site-specific protein labeling inside living cells. *Proc. Natl. Acad. Sci. USA* **107**, 10914–10919 (2010).
- Testa, I. *et al.* Multicolor fluorescence nanoscopy in fixed and living cells by exciting conventional fluorophores with a single wavelength. *Biophys. J.* **99**, 2686–2694 (2010).
- Zhao, Z.W. *et al.* Spatial organization of RNA polymerase II inside a mammalian cell nucleus revealed by reflected light-sheet superresolution microscopy. *Proc. Natl. Acad. Sci. USA* **111**, 681–686 (2014).
- Abrahamsson, S. *et al.* Fast multicolor 3D imaging using aberration-corrected multifocus microscopy. *Nat. Methods* **10**, 60–63 (2013).

13. Chen, J. *et al.* Single-molecule dynamics of enhanceosome assembly in embryonic stem cells. *Cell* **156**, 1274–1285 (2014).
14. Lavis, L.D. & Raines, R.T. Bright ideas for chemical biology. *ACS Chem. Biol.* **3**, 142–155 (2008).
15. Beija, M., Afonso, C.A.M. & Martinho, J.M.G. Synthesis and applications of rhodamine derivatives as fluorescent probes. *Chem. Soc. Rev.* **38**, 2410–2433 (2009).
16. Lavis, L.D. & Raines, R.T. Bright building blocks for chemical biology. *ACS Chem. Biol.* **9**, 855–866 (2014).
17. Gautier, A. *et al.* An engineered protein tag for multiprotein labeling in living cells. *Chem. Biol.* **15**, 128–136 (2008).
18. Lukinavičius, G. *et al.* A near-infrared fluorophore for live-cell super-resolution microscopy of cellular proteins. *Nat. Chem.* **5**, 132–139 (2013).
19. Mujumdar, R.B., Ernst, L.A., Mujumdar, S.R., Lewis, C.J. & Waggoner, A.S. Cyanine dye labeling reagents: sulfoindocyanine succinimidyl esters. *Bioconjug. Chem.* **4**, 105–111 (1993).
20. Panchuk-Voloshina, N. *et al.* Alexa dyes, a series of new fluorescent dyes that yield exceptionally bright, photostable conjugates. *J. Histochem. Cytochem.* **47**, 1179–1188 (1999).
21. Haugland, R.P., Spence, M.T.Z., Johnson, I.D. & Basey, A. *The Handbook: A Guide to Fluorescent Probes and Labeling Technologies* 10th edn. (Molecular Probes, 2005).
22. Zhang, Z., Revyakin, A., Grimm, J.B., Lavis, L.D. & Tjian, R. Single-molecule tracking of the transcription cycle by sub-second RNA detection. *eLife* **3**, e01775 (2014).
23. Bosch, P.J. *et al.* Evaluation of fluorophores to label SNAP-tag fused proteins for multicolor single-molecule tracking microscopy in live cells. *Biophys. J.* **107**, 803–814 (2014).
24. Grimm, J.B. *et al.* Carbofluoresceins and carborhodamines as scaffolds for high-contrast fluorogenic probes. *ACS Chem. Biol.* **8**, 1303–1310 (2013).
25. Vogel, M., Rettig, W., Sens, R. & Drexhage, K.H. Structural relaxation of rhodamine dyes with different N-substitution patterns: a study of fluorescence decay times and quantum yields. *Chem. Phys. Lett.* **147**, 452–460 (1988).
26. Grabowski, Z.R., Rotkiewicz, K. & Rettig, W. Structural changes accompanying intramolecular electron transfer: focus on twisted intramolecular charge-transfer states and structures. *Chem. Rev.* **103**, 3899–4032 (2003).
27. Song, X., Johnson, A. & Foley, J. 7-Azabicyclo[2.2.1]heptane as a unique and effective dialkylamino auxochrome moiety: demonstration in a fluorescent rhodamine dye. *J. Am. Chem. Soc.* **130**, 17652–17653 (2008).
28. Grimm, J.B. & Lavis, L.D. Synthesis of rhodamines from fluoresceins using Pd-catalyzed C–N cross-coupling. *Org. Lett.* **13**, 6354–6357 (2011).
29. Heilemann, M. *et al.* Subdiffraction-resolution fluorescence imaging with conventional fluorescent probes. *Angew. Chem. Int. Ed. Engl.* **47**, 6172–6176 (2008).
30. Dempsey, G.T., Vaughan, J.C., Chen, K.H., Bates, M. & Zhuang, X. Evaluation of fluorophores for optimal performance in localization-based super-resolution imaging. *Nat. Methods* **8**, 1027–1036 (2011).
31. Ha, T. & Tinnefeld, P. Photophysics of fluorescence probes for single molecule biophysics and super-resolution imaging. *Annu. Rev. Phys. Chem.* **63**, 595–617 (2012).
32. Lukinavičius, G. *et al.* Fluorogenic probes for live-cell imaging of the cytoskeleton. *Nat. Methods* **11**, 731–733 (2014).
33. Loving, G. & Imperiali, B. A versatile amino acid analogue of the solvatochromic fluorophore 4-*N,N*-dimethylamino-1,8-naphthalimide: a powerful tool for the study of dynamic protein interactions. *J. Am. Chem. Soc.* **130**, 13630–13638 (2008).
34. Kubota, Y. & Steiner, R.F. Fluorescence decay and quantum yield characteristics of acridine orange and proflavine bound to DNA. *Biophys. Chem.* **6**, 279–289 (1977).
35. Lee, L.G., Berry, G.M. & Chen, C.-H. Vita Blue: a new 633-nm excitable fluorescent dye for cell analysis. *Cytometry* **10**, 151–164 (1989).
36. Bancaud, A. *et al.* Molecular crowding affects diffusion and binding of nuclear proteins in heterochromatin and reveals the fractal organization of chromatin. *EMBO J.* **28**, 3785–3798 (2009).
37. Bancaud, A., Lavelle, C., Huet, S. & Ellenberg, J. A fractal model for nuclear organization: Current evidence and biological implications. *Nucleic Acids Res.* **40**, 8783–8792 (2012).
38. Speight, L.C. *et al.* Efficient synthesis and *in vivo* incorporation of acridon-2-ylalanine, a fluorescent amino acid for lifetime and Förster resonance energy transfer/luminescence resonance energy transfer studies. *J. Am. Chem. Soc.* **135**, 18806–18814 (2013).
39. Mitronova, G.Y. *et al.* New fluorinated rhodamines for optical microscopy and nanoscopy. *Chemistry* **16**, 4477–4488 (2010).
40. Altman, R.B. *et al.* Cyanine fluorophore derivatives with enhanced photostability. *Nat. Methods* **9**, 68–71 (2012).

ONLINE METHODS

Fluorophore modeling and synthesis. Methods for molecular modeling, organic synthesis and additional characterization can be found in the **Supplementary Note**.

General spectroscopic methods. Fluorescent and fluorogenic molecules for spectroscopy were prepared as stock solutions in DMSO and diluted such that the DMSO concentration did not exceed 1% (v/v). Phosphate-buffered saline (PBS) was at pH 7.4 unless otherwise noted. Commercial compounds for spectroscopy were of the highest quality available and obtained from the following sources: Anaspec (**2**); Promega (**10**); Sigma-Aldrich (**11**, **13**); Life Technologies (**17**); AAT Bioquest (**23**); New England BioLabs (**30**).

UV-Vis and fluorescence spectroscopy. Spectroscopy was performed using 1-cm path length, 3.5-mL quartz cuvettes from Starna Cells or 1-cm path length, 1.0-mL quartz microcuvettes from Hellma. All measurements were taken at ambient temperature (22 ± 2 °C) in 10 mM HEPES, pH 7.3, buffer unless otherwise noted. Absorption spectra were recorded on a Cary Model 100 spectrometer (Varian); reported values for extinction coefficients at λ_{max} (ϵ) are averages ($n = 3$). Fluorescence spectra were recorded on a Cary Eclipse fluorometer (Varian). Normalized spectra are shown for clarity.

Quantum yield determination. All reported quantum yield values were measured in our laboratory under identical conditions using a Quantaurus-QY spectrometer (C11374, Hamamatsu). This instrument uses an integrating sphere to determine photons absorbed and emitted by a sample. Measurements were carried out using dilute samples ($A < 0.1$), and self-absorption corrections⁴¹ were performed using the instrument software. Reported values are averages ($n = 3$).

Dioxane-H₂O titration. Dioxane-H₂O titrations were performed in spectral-grade dioxane (Sigma-Aldrich) and milliQ H₂O. The solvent mixtures contained 0.01% (v/v) triethylamine to ensure the rhodamine dyes were in the zwitterionic form. The absorbance values at λ_{max} were measured on 5 μM samples ($n = 2$) using a quartz 96-well microplate (Hellma) and a FlexStation3 microplate reader (Molecular Devices). Values of dielectric constant (ϵ_r) were as reported⁴².

Multiphoton spectroscopy. The two-photon measurements were performed as previously described^{43,44}. Measurements were taken on an inverted microscope (IX81, Olympus) equipped with a 60 \times , 1.2-NA (numerical aperture) water objective (Olympus). Dye samples were excited with pulses from an 80-MHz Ti:sapphire laser (Chameleon Ultra II, Coherent). Fluorescence collected by the objective was passed through a shortpass filter (720SP, Semrock) and a bandpass filter (550BP200, Semrock), and detected by a fiber-coupled Avalanche Photodiode (APD). Two different APDs were used, one optimized for low noise for fluorescence correlation spectroscopy (FCS) and spectral measurements (SPCM_AQRH-14, PerkinElmer) and the other for precise timing for lifetime measurements (PDF-CCTB, Micro Photon Devices). The focused laser spot size was measured to be 0.420 μm (radius where intensity drops to $1/e^2$). Two-photon

excitation spectra were taken on samples of 1 μM dye in HEPES buffer, using 1 mW of laser power at the sample across the spectral range of 710–1,080 nm. The peak molecular brightness, defined as the maximum detected count rate per emitting molecule, was obtained by determining the fluorescence count rate and the average number of emitting molecules in the beam using FCS⁴³. For FCS measurements, a stock dye solution was diluted to 50 nM in 50 mM HEPES, pH 7.2, and excited at discrete laser powers ranging from 5 to 30 mW, with FCS data acquisition for each power setting taken for 100–200 s. The samples were excited at 830-nm and 1,020-nm laser wavelength (the absorption peaks obtained from two photon excitation spectra). The fluorescence signal detected by the APD at each wavelength and power setting was fed to the autocorrelator (Flex03LQ, Correlator.com), and a computer program recorded the autocorrelation function and average fluorescence counts per second, defined as $\langle F \rangle$. The measured autocorrelation curve was fit to an FCS diffusion model with a Matlab program using a customized code (available upon request), to determine the average number of excited molecules $\langle N \rangle$ in the volume of excitation. The molecular brightness ($\langle \epsilon_p \rangle$) was thus obtained as the rate of fluorescence per excited molecule defined as $\langle \epsilon_p \rangle = \langle F \rangle / \langle N \rangle$ (ref. 43). Increasing the laser intensity initially increases the molecular brightness; however, at a certain point molecular brightness leveled off or started decreasing, indicating photobleaching or saturation of the molecule in the excitation volume. The maximum or peak brightness achieved before photobleaching or saturation represents the useful proxy for the photostability of a fluorophore.

Fluorescence-lifetime spectroscopy. For fluorescence-lifetime measurements, a pulse picker (Model 350-160, ConOptics) was placed in the laser beam to reduce the pulse frequency from 80 MHz to 20 MHz. Samples (2 μM dye diluted in 50 mM HEPES, pH 7.2, H₂O, or CH₃OH) were excited at 830-nm laser wavelength and 6-mW laser power. The emitted light was collected by the fast-timing APD and fed to the single-photon counting board (TimeHarp200, PicoQuant). Timing pulses were obtained from a PIN diode (DET01CFC, Thorlabs) monitoring the 20-MHz pulse train. The temporal impulse response of the system was determined by second harmonic generation of laser pulses using a thin nonlinear crystal in place of a dye sample. The lifetime decay data were fit to a single exponential decay function using a custom Matlab program (available upon request). Lifetime value of the reference fluorescein dye measured using our system was 4.025 ± 0.015 ns (mean \pm s.d., $n = 2$) compared to a literature value of 4.1 ± 0.1 ns (ref. 45).

Measurement of increase in fluorescence of HaloTag ligands 27 and 28 upon reaction with HaloTag protein. Absorbance measurements were performed in 1-mL quartz cuvettes. HaloTag protein was used as a 100 μM solution in 75 mM NaCl, 50 mM Tris-HCl, pH 7.4, with 50% (v/v) glycerol (TBS-glycerol). HaloTag ligands **27** and **28** (5 μM) were dissolved in 10 mM HEPES, pH 7.3, containing 0.1 mg mL⁻¹ CHAPS. An aliquot of HaloTag protein (1.5 equiv) or an equivalent volume of TBS-glycerol blank was added, and the resulting mixture was incubated until consistent absorbance signal was observed (~30 min). Additional HaloTag protein did not elicit an increase in absorbance (not shown). Absorbance scans are averages ($n = 2$).

Cell culture, transfection and labeling. HeLa cells (ATCC) and U2OS cells (ATCC) were cultured in Dulbecco's modified Eagle medium (DMEM; Life Technologies) supplemented with 10% (v/v) fetal bovine serum (FBS; Life Technologies), 1 mM GlutaMAX (Life Technologies) and 1 mM sodium pyruvate (Sigma), and maintained at 37 °C in a humidified 5% (v/v) CO₂ environment. These cell lines undergo regular mycoplasma testing by the Janelia Cell Culture Facility. Cells were transfected with HaloTag-H2B, HaloTag-tubulin, Snap-tag-TetR or Snap-tag-H2B using an Amaxa Nucleofector (Lonza). Before the imaging experiments, transfected cells were transferred onto a no. 1 coverslip (Warner Instruments) that was cleaned by Piranha solution (3:1 (v/v) mixture of concentrated H₂SO₄ and 30% (v/v) hydrogen peroxide). To label live cells with the HaloTag or Snap-tag ligands, we added compounds **9**, **10**, **27**, **28**, **29**, **30**, or **31** to the growth medium, and the samples were incubated for 15 min. Labeling concentrations were typically 100–500 nM for confocal, wide-field, and dSTORM experiments and 5–50 nM for single-molecule tracking experiments. Cells were then washed briefly with PBS (1×) and then incubated in DMEM-FBS for an additional 15 min. Before imaging, the cells were washed briefly with PBS (3×) and placed in fresh DMEM-FBS for imaging. All washes were omitted in the 'no wash' experiments. For nuclear staining, cells were incubated in PBS for 5 min (2×) and then in PBS containing 5 μM DRAQ5 (Cell Signaling) for 5 min, followed by a brief wash with PBS (1×). During all imaging experiments, cells were maintained at 37 °C in a humidified 5% CO₂ environment supplied by a live-cell incubator (Tokai Hit).

Microscopy hardware. Three separate systems were used to acquire microscopic images. Confocal microscopy was performed using a Zeiss LSM 510 Meta confocal microscope with an LD C-Apochromat 40×, 1.2 W Korr M27 UV-VIS-IR objective. Wide-field microscopy, 2D single-molecule tracking and super-resolution imaging experiments were conducted on a Nikon Eclipse Ti wide-field epifluorescence microscope equipped with a 100×, 1.4-NA oil-immersion objective lens (Nikon), a Lumencor light source, a set of lasers (405 nm/100 mW, Coherent Cube; 561 nm/200 mW, Cobolt Jive; 633 nm/140 mW, Vortran Stradus), controlled by an Acousto-Optic Tunable Filter (AA Opto-Electronic), two filter wheels (Lambda 10-3, Sutter Instruments), a perfect focusing system (Nikon) and an EMCCD (electron-multiplying charge-couple device) camera (iXon3, Andor). Emission filters (FF01 593/40 or FF01 676/37, Semrock) were placed in front of the cameras for JF₅₄₉ and JF₆₄₆ emission. A multiband mirror (405/488/561/633 BrightLine quad-band bandpass filter, Semrock) was used to reflect the excitation laser beams into the objective. The microscope, cameras and hardware were controlled through the NIS-Elements software (Nikon). Other live-cell single super-resolution imaging experiments were recorded on a custom-built three-camera RAMM frame (ASI) microscope using an 1.4-NA PLAPON 60× OSC objective (Olympus), and a 300-mm focal length tube lens (LAO-300.0, Melles Griot), resulting in 100× overall magnification. Stroboscopic 405-nm excitation of the Stradus 405-100 laser (Vortran) was achieved using a NI-DAQ-USB-6363 acquisition board (National Instruments), which also controlled the 637-nm laser emission from a Stradus 637-140 laser (Vortran). A 2-mm-thick quad-band dichroic (ZT 405/488/561/640rpx, Chroma), and a bandpass emission filter (FF01-731/137-25,

Semrock) filtered the emitted light. Fluorescence was detected with a back-illuminated EMCCD camera (Andor Technology, Ixon Ultra DU-897U-CS0-EXF, 17-MHz EM amplifier), which was controlled through μManager (v. 1.4.17).

dSTORM imaging. Super-resolution imaging experiments were performed on live samples (Fig. 2j and Supplementary Figs. 2c and 4d,g) and fixed cells (Figs. 1i and 2b and Supplementary Figs. 2a and 4a). For live-cell dSTORM imaging the cells were labeled, washed and imaged directly in DMEM-FBS. For fixed-cell preparations, cells were labeled, washed and fixed in 4% paraformaldehyde (Electron Microscopy Sciences) in PBS buffer (pH 7.5). The cells were imaged in a sealed cell chamber (Life Technologies) containing nitrogen-degassed redox buffer consisting of PBS supplemented with 50 mM mercaptoethylamine (Sigma-Aldrich), 10% (w/v) glucose, 0.5 mg mL⁻¹ glucose oxidase (Sigma-Aldrich) and 28,400 U mL⁻¹ catalase (Sigma-Aldrich). Before imaging, JF₅₄₉ could be efficiently 'shelved' in a dark state upon illumination with 2 kW cm⁻² of excitation light (561 nm) and then activated back to a fluorescent state by blue light (405 nm) with low intensity (~20 W cm⁻²). JF₆₄₆ fluorophores were converted into a predominantly dark state using continuous illumination of 637-nm excitation light at 14 kW cm⁻², after which individual rapidly blinking molecules of JF₆₄₆ fluorophores were observed. These experiments were conducted on the two wide-field microscope systems described above: the Nikon Eclipse Ti epifluorescence microscope (Figs. 1i and 2j and Supplementary Figs. 2a,c and 4g) and the custom-built three-camera microscope with an ASI RAMM frame (Fig. 2b and Supplementary Fig. 4a,d).

dSTORM analysis. The spot localization (*x*, *y*) was obtained on the basis of the multiple-target tracing (MTT) algorithm^{46,47} using a custom Matlab program (available upon request). For each frame, the point spread function (PSF) of individual fluorophores was fitted into 2D Gaussian distribution. Integrated fluorescence intensities were calculated and converted to photon counts using analysis routines written in Igor Pro version 6.34A (available upon request). Localization errors were calculated using equation (6) in Mortensen *et al.*⁴⁸. Super-resolution images were rendered using the software package Localizer by Dedecker *et al.*⁴⁹ running from Igor Pro v. 3.34A, which superimposes the position coordinates of detected spots as Gaussian masks using the fitted intensity values as amplitudes and the localization errors as the widths. The dSTORM data for experiments comparing two different fluorophore ligands were recorded on the same day under identical illumination conditions.

Two-color single-molecule experiments. The two-color single-molecule experiments were recorded on the Nikon Eclipse Ti wide-field epifluorescence microscope. We first performed a 2D single-molecule tracking of Snap-tag-TetR-JF₅₄₉ using a 561-nm laser of excitation intensity ~1 kW cm⁻² at a frame rate of 100 Hz. Immediately after the completion of the single-particle tracking experiment, we then imaged HaloTag-H2B-JF₆₄₆ under the dSTORM mode as described above. Transmission images were taken before and after the tracking dSTORM experiments, and a cross-correlation algorithm was employed to calculate the image drift⁵⁰. Tracking analysis of TetR was performed using the commercial tracking software DiaTrack (v. 3.03, Semasopht), which

identifies and fits the intensity spots of fluorescent particles with 2D Gaussian functions matched to the experimentally determined PSF. The diffusion map was created using tracking routines written in Igor Pro 6.34A, calculating the local apparent diffusion of TetR mobility evaluated on a 20 nm × 20 nm *xy* grid from the mean square displacements over a timescale of 10 ms (**Fig. 2j**; code is available upon request). Whenever two or more separate displacements originating within 80 nm of a given grid node were found, a local apparent diffusion coefficient was calculated and plotted. We then selected H2B clusters as the 500 brightest spots in the super-resolved image. From this analysis, we generated a histogram of apparent diffusion coefficients for all trajectories that dwelled within 320 nm of a H2B cluster for at least 10 ms. We then plotted histograms of the diffusion coefficient of both the H2B-colocalized and the noncolocalized TetR trajectories (**Supplementary Fig. 4h**).

41. Suzuki, K. *et al.* Reevaluation of absolute luminescence quantum yields of standard solutions using a spectrometer with an integrating sphere and a back-thinned CCD detector. *Phys. Chem. Chem. Phys.* **11**, 9850–9860 (2009).
42. Critchfield, F.E., Gibson, J.A. Jr. & Hall, J.L. Dielectric constant for the dioxane–water system from 20 to 35°. *J. Am. Chem. Soc.* **75**, 1991–1992 (1953).
43. Mütze, J. *et al.* Excitation spectra and brightness optimization of two-photon excited probes. *Biophys. J.* **102**, 934–944 (2012).
44. Akerboom, J. *et al.* Optimization of a GCaMP calcium indicator for neural activity imaging. *J. Neurosci.* **32**, 13819–13840 (2012).
45. Magde, D., Rojas, G.E. & Seybold, P.G. Solvent dependence of the fluorescence lifetimes of xanthene dyes. *Photochem. Photobiol.* **70**, 737–744 (1999).
46. Sergé, A., Bertaux, N., Rigneault, H. & Marguet, D. Multiple-target tracing (MTT) algorithm probes molecular dynamics at cell surface. *Protoc. Exch.* doi:10.1038/nprot.2008.128 (2008).
47. Sergé, A., Bertaux, N., Rigneault, H. & Marguet, D. Dynamic multiple-target tracing to probe spatiotemporal cartography of cell membranes. *Nat. Methods* **5**, 687–694 (2008).
48. Mortensen, K.I., Churchman, L.S., Spudich, J.A. & Flyvbjerg, H. Optimized localization analysis for single-molecule tracking and super-resolution microscopy. *Nat. Methods* **7**, 377–381 (2010).
49. Dedecker, P., Duwé, S., Neely, R.K. & Zhang, J. Localizer: fast, accurate, open-source, and modular software package for superresolution microscopy. *J. Biomed. Opt.* **17**, 126008 (2012).
50. Guizar-Sicairos, M., Thurman, S.T. & Fienup, J.R. Efficient subpixel image registration algorithms. *Opt. Lett.* **33**, 156–158 (2008).